

IPTC-21884-MS

Digital Rock Reconstruction Using Wasserstein GANs with Gradient Penalty

Yiteng Li, Xupeng He, and Weiwei Zhu, King Abdullah University of Science and Technology; Marwa AlSinan and Hyung Kwak, Saudi Aramco; Hussein Hoteit, King Abdullah University of Science and Technology

Copyright 2022, International Petroleum Technology Conference DOI [10.2523/IPTC-21884-MS](https://doi.org/10.2523/IPTC-21884-MS)

This paper was prepared for presentation at the International Petroleum Technology Conference held in Riyadh, Saudi Arabia, 21-23 February 2022.

This paper was selected for presentation by an IPTC Programme Committee following review of information contained in an abstract submitted by the author(s). Contents of the paper, as presented, have not been reviewed by the International Petroleum Technology Conference and are subject to correction by the author(s). The material, as presented, does not necessarily reflect any position of the International Petroleum Technology Conference, its officers, or members. Papers presented at IPTC are subject to publication review by Sponsor Society Committees of IPTC. Electronic reproduction, distribution, or storage of any part of this paper for commercial purposes without the written consent of the International Petroleum Technology Conference is prohibited. Permission to reproduce in print is restricted to an abstract of not more than 300 words; illustrations may not be copied. The abstract must contain conspicuous acknowledgment of where and by whom the paper was presented. Write Librarian, IPTC, P.O. Box 833836, Richardson, TX 75083-3836, U.S.A., fax +1-972-952-9435.

Abstract

Due to the scarcity and vulnerability of physical rock samples, digital rock reconstruction plays an important role in the numerical study of reservoir rock properties and fluid flow behaviors. With the rapid development of deep learning technologies, generative adversarial networks (GANs) have become a promising alternative to reconstruct complex pore structures. Numerous GAN models have been applied in this field, but many of them suffer the unstable training issue. In this study, we apply the Wasserstein GAN with gradient penalty, also known as the WGAN-GP network, to reconstruct Berea sandstone and Ketton limestone. Unlike many other GANs using the Jensen-Shannon divergence, the WGAN-GP network exhibits a stable training performance by using the Wasserstein distance to measure the difference between generated and real data distributions. Moreover, the generated image quality correlates with the discriminator loss. This provides us an indicator of the training state instead of frequently subjective assessments in the training of deep convolutional GAN (DCGAN) based models. An integrated framework is presented to automate the entire workflow, including training set generation, network setup, model training and synthetic rock validation. Numerical results show that the WGAN-GP network accurately reconstructs both Berea sandstone and Ketton limestone in terms of two-point correlation and morphological properties.

Introduction

Evaluation of rock properties and fluid flow behaviors in rock samples provides valuable information to set up parameters for large-scale reservoir simulation (Geiger et al., 2010; He, Sinan, et al., 2021; Hoteit & Firoozabadi, 2008a, 2008b). However, apart from prohibitive acquisition cost, physical rock samples are risky to be damaged during core flooding experiments. This makes it impractical to use a single rock for different research purposes. In addition, the heterogeneous nature of pore structures brings significant uncertainties through limited rock samples. Thus, it is necessary to have a sufficient number of similar pore structures to fully investigate rock and transport properties in a given rock. Such demands stimulate the development of digital rock reconstruction techniques.

Conventionally, there are three types of methods to create digital pore structures. The most straightforward approach is direct scanning of rock samples using sophisticated imaging tools, such as

micro-CT (Bostanabad et al., 2018; Flannery et al., 1987), Nano-CT (Chen et al., 2013), FIB-SEM (Bera et al., 2018; Tahmasebi et al., 2015; Tahmasebi, 2018), etc. However, direct imaging methods simply digitize the porous structure under study, and they cannot generate replicas with similar geometry properties. Another class of methods is the stochastic method, using the geostatistics information, e.g., multiple-point statistics (Okabe and Blunt, 2004; Okabe and Blunt, 2007). A variety of multiple-point statistics methods have been proposed, including cross-correlation-based simulation (Tahmasebi and Sahimi, 2013), direct sampling method (Mariethoz et al., 2019), single normal equation simulation (Strebel, 2002), hybrid pattern-pixel-based simulation (Tahmasebi, 2017), etc. In addition, digital pore structures can be generated by simulating geological processes, including sedimentation, compaction, and diagenesis (Bryant et al. 1993; Coelho et al. 1997; Øren, P.E. and Bakke, 2003). Such methods are known as process-based methods.

Recent advances in machine learning have inspired various environmental, geoscience, and energy applications, such as CO₂ leakage forecasting in saline aquifers (He, Zhu, et al., 2021a), history matching in field-scale simulations (Santoso et al., 2021), upscaling of discrete-fracture models (He et al., 2020; He, Santoso, et al., 2021), upscaling of rock fractures (He, Zhu, et al., 2021b), recovery factor prediction in gas-injected reservoirs (He, Qiao, et al., 2021), multi-component flash calculations (Li et al., 2019; Zhang et al., 2020) and recognizing and detecting fractures from real outcrop (Santoso et al., 2019). These successful implementations motivate us to explore the possible employment of machine learning on digital rock reconstructions. Generative Adversarial Networks (GANs), first proposed by Ian Goodfellow et al. (2015), have been extensively applied to pore-scale imaging and processing (Wang et al., 2021), such as image segmentation, resolution enhancement, image reconstruction, etc. Due to the strong feature learning capability, GANs are suitable for synthetic rock reconstruction without losing diversity by implicitly learning the probability distribution from the training dataset. Mosser et al. (2017) firstly used DCGANs to reconstruct 3D porous structures of sandstone and carbonate. After their ground-breaking work, DCGANs rapidly swept the community and became an important approach for digital rock reconstruction (Mosser et al., 2018; Liu et al., 2019; Volkhonskiy et al., 2019; Valsecchi et al., 2020). Inspired by this, various GAN models have also been used, including but not limited to conditional GAN (Feng et al., 2019; Volkhonskiy et al., 2019), style GAN (Fokina et al., 2020), progressively growing GAN (Zheng and Zhang, 2020), Bicycle GAN (Feng, et al., 2020), as well as some hybrid models combining variational autoencoder and DCGAN (Shams et al., 2020; Zhang et al., 2021; Zhang et al., 2021).

Even though GANs have achieved great success in digital rock reconstruction, many of them suffer the unstable training issue. This roots in the fact that these networks use the Jensen-Shannon (JS) divergence to evaluate the distance between generated and real data distributions. Unfortunately, the JS divergence remains constant if the real and generated data distributions have no overlap. Under such circumstances, it cannot provide useful gradients to update generator parameters and consequently the training process becomes unstable. We note that a collection of tricks can be used to stabilize GANs training, such as one-sided label smoothing, white noise injection, etc., but they fail to resolve the fundamental issue. Thus, Arjovsky et al. (2017) proposed the Wasserstein GAN (WGAN) by replacing the JS divergence with the distance of Wasserstein to enhance the stable training process. The Lipschitz constraint is conserved by weight clipping in their networks, yet it is prone to cause the gradient vanishing or gradient exploding issue. To overcome this issue, Gulrajani et al. (2017) subsequently improved WGANs by introducing a gradient penalty to conserve the Lipschitz constraint instead of weight clipping. One distinct advantage of WGAN-type models is that the loss of discriminator correlates with the quality of generated images well. Thus, it allows us to track the training state more easily and greatly reduces the subjective assessment via visual check of generated images.

Due to these advantages, in this study, we train WGAN-GP networks to reconstruct Berea sandstone and Ketton limestone from 2D image datasets. The training dataset is subsampled from the original binary images and then augmented by applying rotation, as well as slightly horizontal/vertical shear transformation.

We present an integrated framework to automate the whole process from training set generation, network setup to model training, and synthetic image validation. Synthetic rock images are examined in terms of the two-point correlation and Minkowski functionals, and then they can be collected based on a certain property range, like porosity. Even though we can achieve the same purpose by training conditional GANs with a porosity constraint, here are a couple of concerns. First, the literature review shows that current conditional GANs require the porosity of generated rocks approaching a reference porosity value, but in practice, it is often expected that the porosity of generated rocks is bounded by a certain range. In addition, the objective function of the generator has to include an additional contribution from the porosity constraint. However, selecting the penalty coefficient for this porosity constraint is heuristic, which will increase the difficulty in training a conditional GAN by trial and error. In some literature, the penalty coefficient of the porosity constraint is regarded as a hyperparameter, and it is assumed constant. However, this may lead to a failure of training in our experiments. Instead, the coefficient should dynamically change with the training process, which requires a sophisticated algorithm to control the adjustment of this coefficient. From the perspective of engineering applications, the proposed workflow is simple and robust to generate synthetic rock images under a given rock property within any range of interest.

The rest of this paper is organized as follows. In the next section, we briefly describe the WGAN-GP network. Then an integrated workflow is presented, which automates the entire process consisting of training image preparation, model training, and synthetic rock validation. We will conduct numerical experiments to reconstruct Berea sandstone and Ketton limestone using the WGAN-GP networks and then evaluate synthetic rocks by comparing the two-point correlation and morphological properties of real and generated images. In the end, we will make concluding remarks and present some future works.

Wasserstein GAN with Gradient Penalty

Typically, GANs include two critical components, discriminator and generator. During the training process, the discriminator and generator compete with each other. In particular, the discriminator attempts to discern generated images from real images, while the generator tries to create "real" images as much as possible to fool the discriminator. Let us denote the discriminator and generator by D_ϕ and G_θ , respectively. Suppose that the real dataset \mathbf{x} is sampled from P_{Data} . The random noise \mathbf{z} from a normal distribution P_z is fed into the generator to create rock images after a series of deep convolutional operations. For GANs using the JS divergence to measure the distance between generated and real data distributions, the discriminator serves as a binary classifier with real images labeled by one and generated images labeled by zero. Thus, the two-player game between discriminator and generator can be formulated as the following min-max optimization problem

$$\min_{\theta} \max_{\phi} \mathbb{E}_{\mathbf{x} \sim P_{\text{Data}}} [\log(D_\phi(\mathbf{x}))] + \mathbb{E}_{\mathbf{z} \sim P_z} [\log(1 - D_\phi(G_\theta(\mathbf{z})))] \quad (1)$$

where \mathbb{E} calculates the expected value, Eq. (1) is solved by seeking for an optimal set of discriminator parameters ϕ to maximize the binary cross-entropy (BCE) of discriminator predictions given the generator parameters are fixed. Then the generator parameters θ are updated by minimizing the BCE of $-\mathbb{E}[\log(D_\phi(G_\theta(\mathbf{z})))]$, rather than $\mathbb{E}[\log(1 - D_\phi(G_\theta(\mathbf{z})))]$ for numerical concern, with the updated discriminator parameters. This training process proceeds by training D_ϕ and G_θ in sequence using the gradient-descent method until training is completed.

In comparison, the objective function of the WGAN-GP network has the following form (Gulrajani et al., 2017)

$$\min_{\theta} \max_{\phi} \mathbb{E}_{\mathbf{z} \sim P_z} [D_\phi(G_\theta(\mathbf{z}))] + \mathbb{E}_{\mathbf{x} \sim P_{\text{Data}}} [D_\phi(\mathbf{x})] + \lambda \mathbb{E}_{\hat{\mathbf{x}} \sim P_{\hat{\mathbf{x}}}} \left[\left(\|\nabla_{\hat{\mathbf{x}}} D(\hat{\mathbf{x}})\|_2 - 1 \right)^2 \right] \quad (2)$$

where λ is the penalty coefficient and it is set to 10 in practical applications. Similarly, we will minimize L_D and L_G to optimize parameters of discriminator and generator, respectively

$$L_D = \mathbb{E}[D_\phi(G_\theta(z))] - \mathbb{E}[D_\phi(x)] + \lambda \mathbb{E}[\|\nabla_{\hat{x}} D(\hat{x})\|_2 - 1]^2 \quad (3)$$

$$L_G = -\mathbb{E}[D_\phi(G_\theta(z))] \quad (4)$$

In Eq. (3), the interpolated image \hat{x} is a linear combination of the real image x and generated image $\tilde{x} = G_\theta(z)$

$$\hat{x} = \epsilon * x + (1 - \epsilon) * \tilde{x},$$

where $\epsilon \in (0, 1)$ is a random number sampled from the uniform distribution. Instead of training the discriminator and generator one by one in DCGANs, we train the discriminator in the WGAN-GP network five times and then update the generator once. Moreover, batch normalization is removed from the discriminator to ensure the accuracy of gradient penalty with respect to the inputs, as suggested by Zheng and Zhang (2020).

Proposed Workflow

To automate the entire process of digital rock reconstruction, an integrated workflow is presented, which consists of three main steps: training set generation, model training, and synthetic image validation, as shown in Figure 1. We will give a detailed description of each of the steps in the following content.

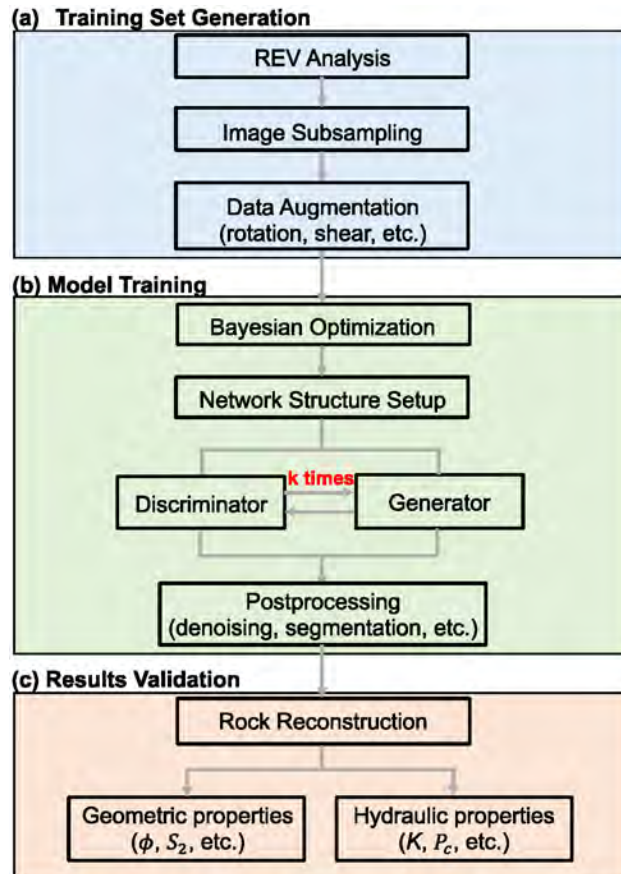


Figure 1—Illustration of workflow to automate digital rock reconstruction.

Training set generation

In this study, we used the Berea sandstone and Ketton limestone images to train our WGAN-GP network. For illustration purposes, 2D binary images are used as training input, but this doesn't affect the extension of the proposed workflow to reconstruct 3D porous structures. To have a sufficient training dataset, we first create the training set by subsampling the original binary image. For the Berea sandstone, the kernel size is set to 64×64 pixels² with a stride size of 8 pixels. For the Ketton limestone, the original image is first downsampled from 500×500 pixels² to 256×256 pixels² in order to capture pores and grains in the Ketton limestone (Mosser et al., 2017). Similarly, we use a kernel size of 64×64 pixels² with a smaller moving stride of 4 pixels to extract subvolumes as the initial training dataset. To further augment our dataset, the training image is rotated by an angle, randomly sampled from a uniform distribution between 0 to 360 degrees. In addition, the pore structure is also slightly transformed by applying a horizontal or vertical shear angle which is uniformly distributed within $[-10, 10]$ degree. The augmented dataset will be used to train the WGAN-GP network. We will shuffle the entire dataset once all mini-batches are iterated over.

Model Training

Figure 2 shows the network architecture of our WGAN-GP model. To synthesize a scalable image, we adopt fully convolutional architectures for the generator. Particularly, the generator has X blocks, the first five of which are composed of the transposed convolution layer, batch normalization layer, and ReLU activation layer. Each transposed convolution layer uses a kernel size of 3×3 and stride size of 2. As the transposed convolution layer goes deeper and deeper, the size of feature maps is enlarged by a factor of 2, while the number of filters is half of that in the precedent layer. The last transposed convolution layer of the generator is followed by a hyperbolic tangent activation function such that output values are bounded between -1 and 1 .

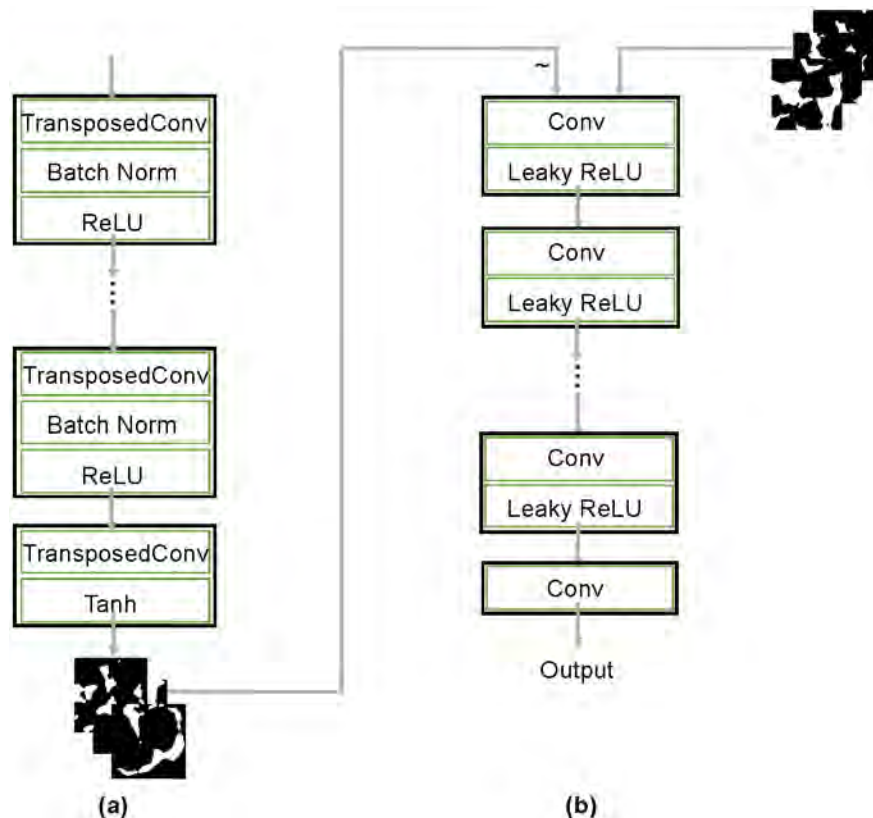


Figure 2—Network architectures of (a) generator and (b) discriminator.

On the other hand, the discriminator has Y convolution layers with a kernel size of 3×3 and a stride size of 2. After each convolution layer, the image size is reduced by half, and accordingly, the number of filters doubles. As mentioned in the last section, we remove the batch normalization layer to preserve the accuracy of the gradient penalty. Therefore, the first four convolution layers are followed by the leaky ReLU activation function immediately, and the last convolution layer directly outputs the result. The detailed layer setup in the generator and discriminator are summarized in Table 1.

Table 1—Network Architecture of the generator and discriminator.

Block	Type	Filters	Kernel Size	Stride	Batch Normalization	Activation
Generator						
1	TransposedConv	512	3×3	4	Yes	ReLU
2	TransposedConv	256	3×3	2	Yes	ReLU
3	TransposedConv	128	3×3	2	Yes	ReLU
4	TransposedConv	64	3×3	2	Yes	ReLU
5	TransposedConv	64	3×3	2	Yes	ReLU
6	TransposedConv	1	3×3	1	No	Tanh
Discriminator						
1	Conv	64	3×3	2	No	Leaky ReLU
2	Conv	128	3×3	2	No	Leaky ReLU
3	Conv	256	3×3	2	No	Leaky ReLU
4	Conv	512	3×3	2	No	Leaky ReLU
5	Conv	1	4×4	1	No	None

To train our WGAN-GP networks, the adam optimizer is used with the learning rate of 2×10^{-4} . The dimension of latent input is set to 100, and the mini-batch size is 64. For the leaky ReLU activation function, the negative slope coefficient is 0.2. The WGAN-GP networks are trained in a scheme that the discriminator is updated 5 times after one update of the generator. Totally, we train our model for 10000 generator updates. Images generated by the WGAN-GP network are then post-processed by rescaling grayscale values to [0 1] Removing single-pixel noise using a 3×3 median filter and binarizing the resultant image with Otsu's method (Otsu, 1979).

Results Validation

As a successful digital rock reconstruction method, the reconstructed pore structures are supposed to be diversified with similar geometrical and hydraulic properties to the given rock sample. In order to evaluate the generative performance, in this study, we calculate geometrical properties of synthetic rock images, including the two-point correlation and three Minkowski functionals, and compare them with the real dataset. The two-point correlation S_2 characterizes the probability that two points \mathbf{x} and $\mathbf{x}+\mathbf{r}$, separated by a distance of r , are located in the pore space

$$S_2(\mathbf{r}) = \mathbf{P}(\mathbf{x} \in P, \mathbf{x} + \mathbf{r} \in P), \text{ for } \mathbf{x}, \mathbf{r} \in \mathbb{R}^d. \quad (5)$$

On the other hand, Minkowski functionals are often used to describe the morphological characteristics of pore structures, which are correlated with transport properties. For a 2D binary image, we can estimate the area of pore phase, equivalent to porosity in 2D, the circumference, and 2D Euler characteristic in terms of the zeroth-, first- and second-order Minkowski functionals, respectively. A detailed description regarding

the calculation of Minkowski functionals on the 2D binary image can be found in the reference (Legland et al., 2007).

Numerical Results

We first trained a WGAN-GP network to reconstruct the pore structures of Berea sandstone. To visualize the generator performance, we compare 25 images randomly sampled from the training dataset to synthetic images in Figure 3, with the size of 64×64 pixels². Overall, the generated samples capture the pore structures of the training samples. Figure 4 shows two-point correlation functions of 100 training and reconstructed Berea sandstone images, both of which are not scaled by porosity. The shaded area is plotted at one standard deviation with the center of mean values. It can be seen the two-point correlation functions of the generated images agree with those of the original images very well. Figure 5 shows the box plots for three Minkowski functionals, namely (a) area, (b) circumference, and (c) 2D Euler characteristic of 100 training and synthetic images. As we can see, three Minkowski functionals exhibit good agreement between the training and reconstructed samples. On the other hand, the generated images show a wide range of Minkowski functionals, implying the trained WGAN-GP network enables the generation of diverse pore structures yet with similar morphological features to the original images. We also use the trained WGAN-GP network to generate synthetic Berea sandstone images with the size of 128×128 pixels², which is shown in Figure 6.

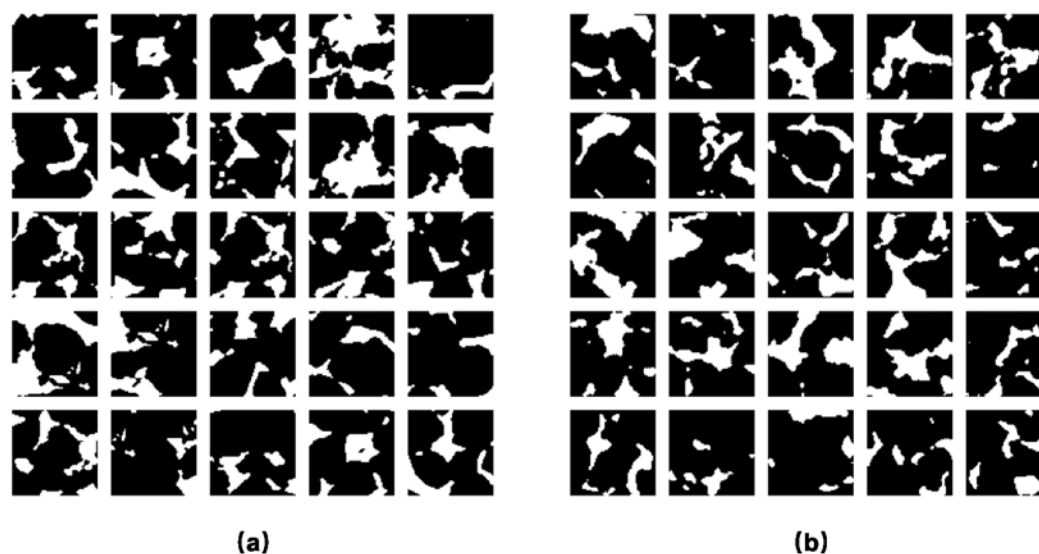


Figure 3—Twenty-five images of Berea sandstone for training (a) and synthetic images given by the generator (b).

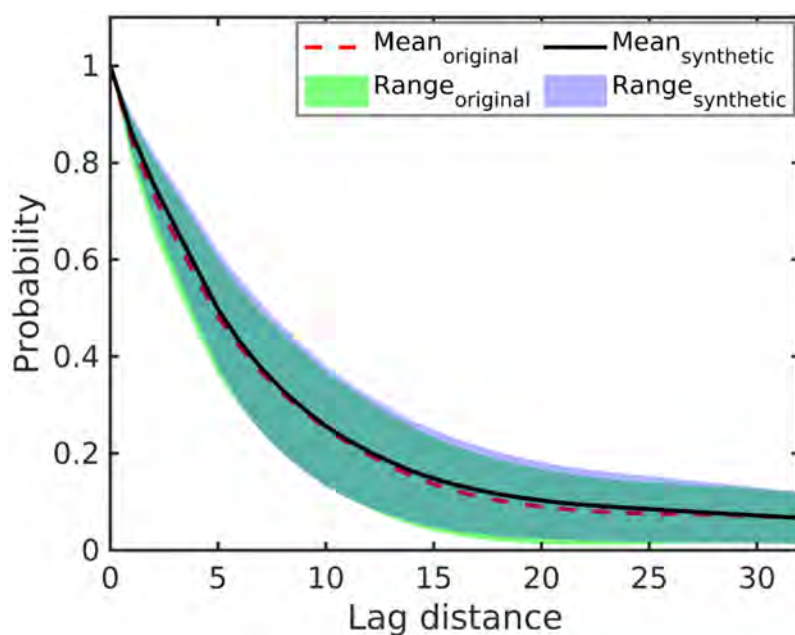


Figure 4—Comparison of two-point correlation functions for 100 training and synthetic Berea sandstone images, respectively.

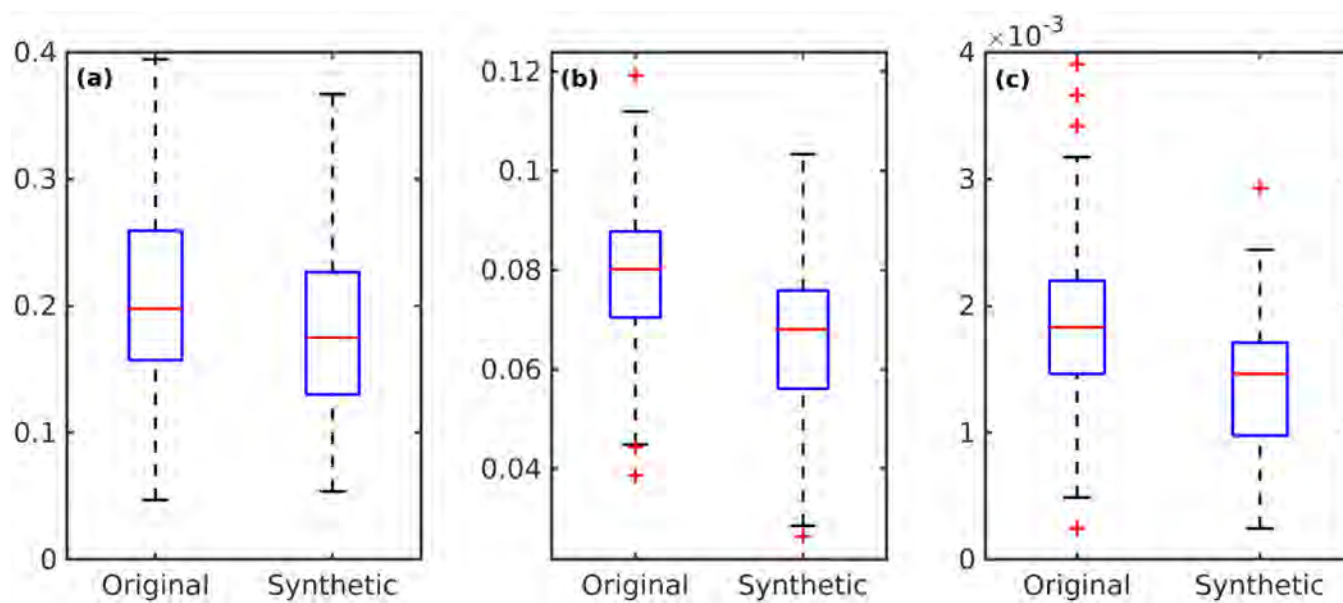


Figure 5—Comparison of Minkowski functionals for 100 training and synthetic Berea sandstone images, (a) area (porosity), (b) circumference, and (c) 2D Euler characteristic.

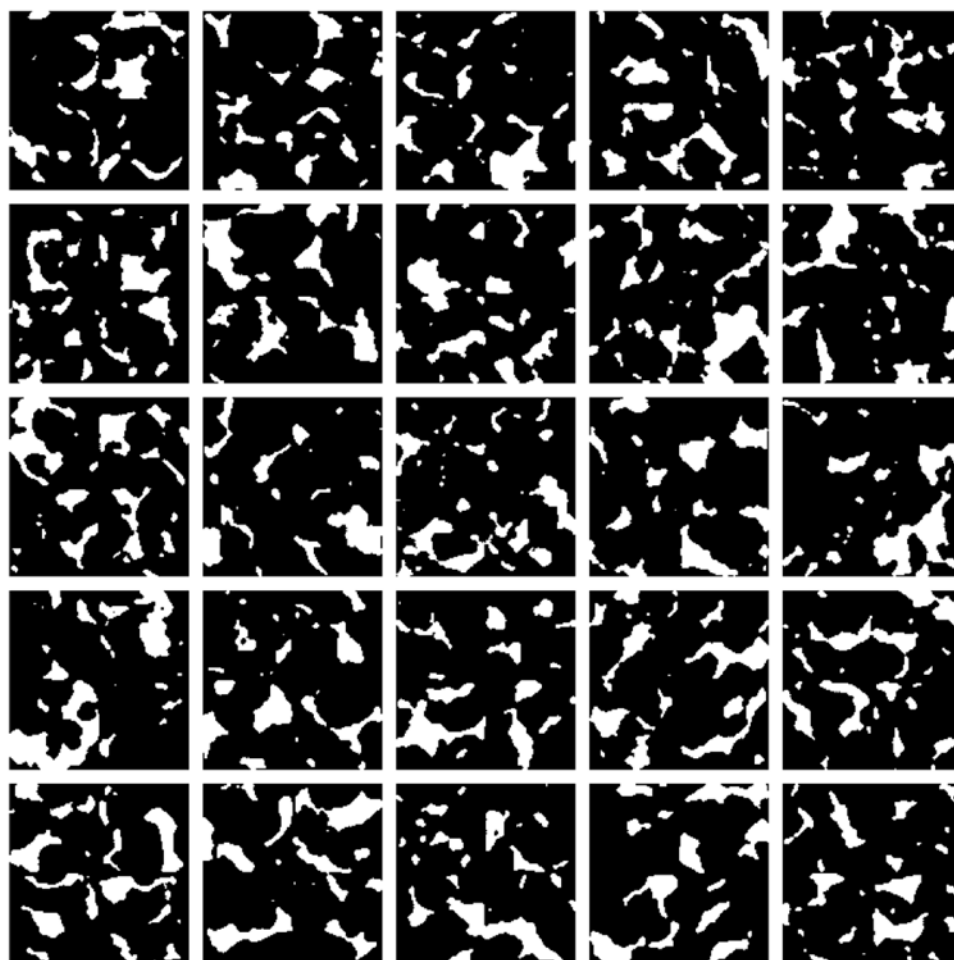


Figure 6—Twenty-five reconstructed Berea sandstone samples with a size of 128×128 pixels².

Another WGAN-GP network is trained to reconstruct Ketton limestone. Similarly, the generative performance is examined in Figure 7 by comparison of the synthetic images, with the size of 64×64 pixels², to the training images. Then we calculate the two-point correlation functions, as shown in Figure 8. Figure 9 compares three Minkowski functionals of 100 training and synthetic Ketton limestone samples. In comparison to Berea sandstone, the median porosity of reconstructed samples has a distinct decline. This may be attributed to that the shear transformation reduces porosities of training images for Ketton limestone more significantly than Berea sandstone. In general, the results show that the synthetic images show good agreement with the original images without losing diversity. Figure 10 displays the generated Ketton limestone images with the size of 128×128 pixels², which pronouncedly shows the hole effect as the result of large grains.

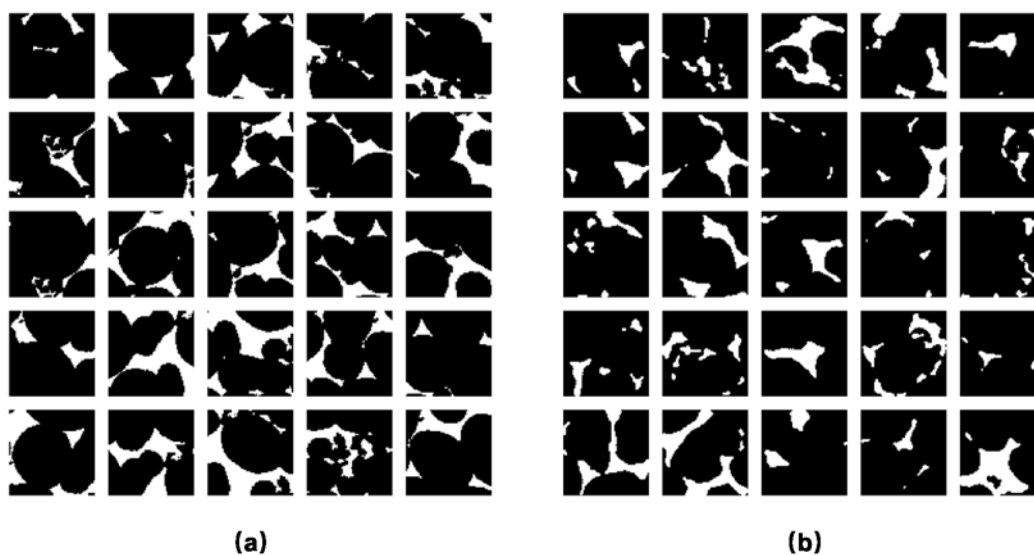


Figure 7—Twenty-five images of Ketton limestone for training (a) and synthetic images given by the generator (b).

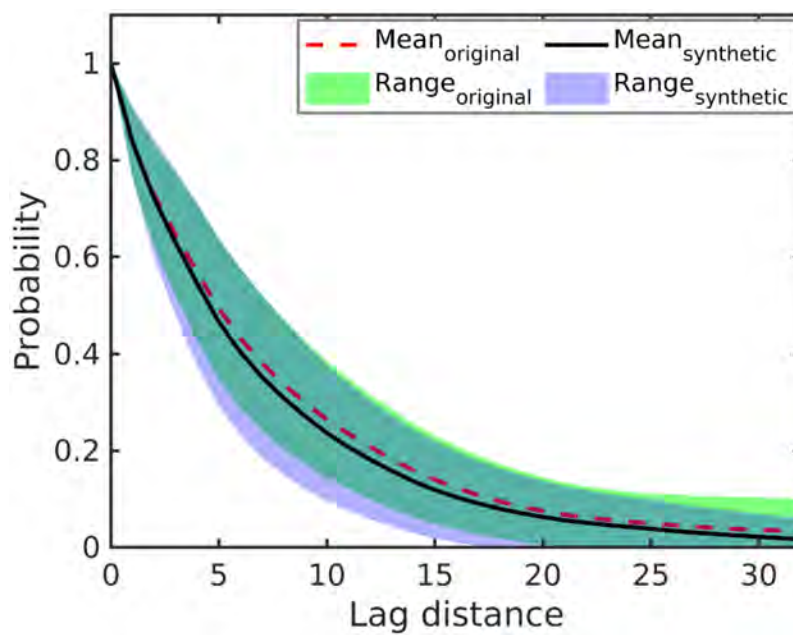


Figure 8—Comparison of two-point correlation values for 100 training and synthetic Ketton limestone images.

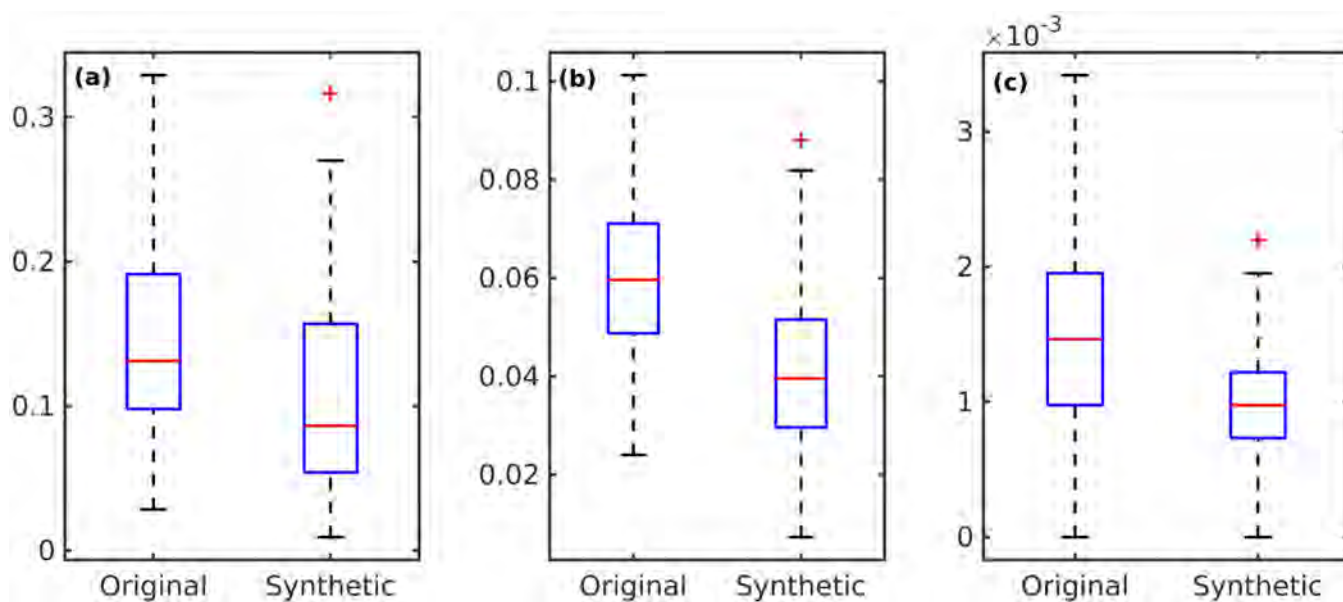


Figure 9—Comparison of Minkowski functionals for 100 training and synthetic Ketton limestone images, (a) area (porosity), (b) circumference, and (c) 2D Euler characteristic.

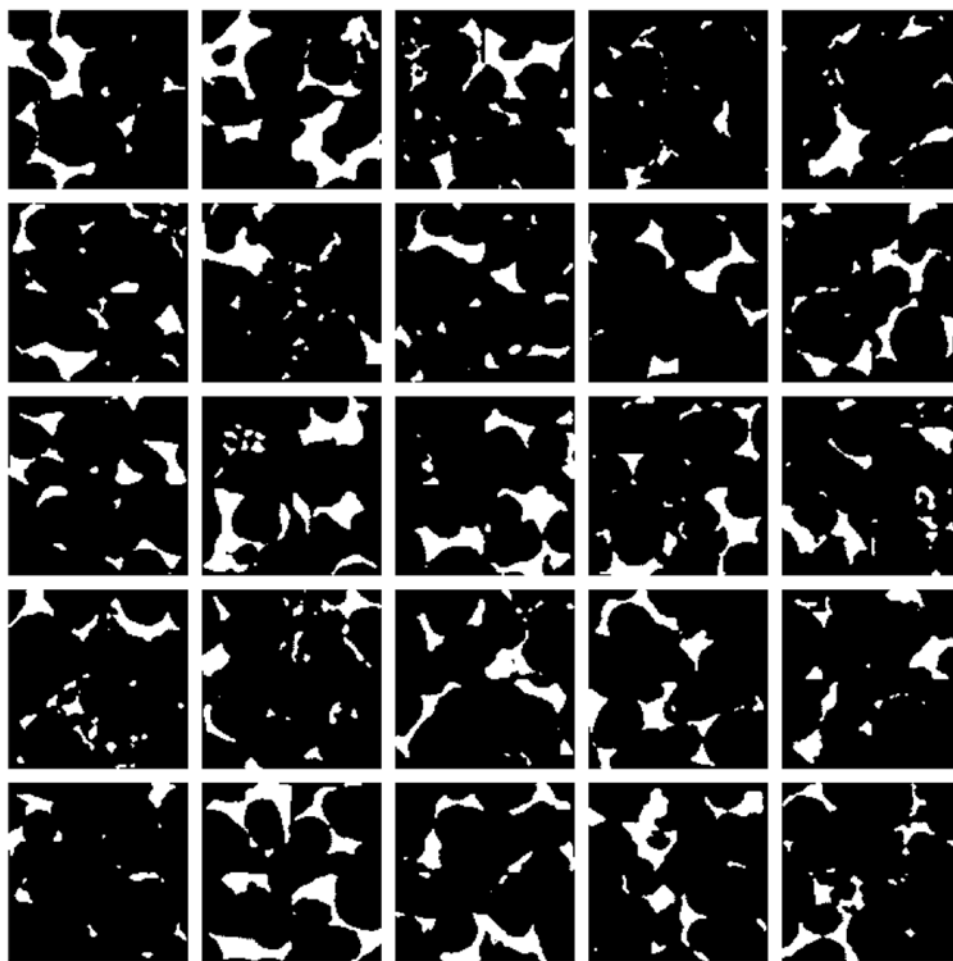


Figure 10—Twenty-five reconstructed Ketton limestone samples with a size of 128×128 pixels².

Conclusion and Future Works

In this study, WGAN-GP networks are trained to reconstruct Berea sandstone and Ketton limestone. The training dataset is augmented by random rotation and shear transformation of the initial training samples. However, unlike random rotation of training images, the shear transformation could change pore structures and consequently affect the training process. An integrated framework is presented to automate the entire workflow, including training set generation, Network setup, model training, and synthetic rock validation. We evaluated the generated Berea sandstone and Ketton limestone images in terms of the two-point correlation and Minkowski functionals. It is found that WGAN-GP networks could reproduce pore structures without losing diversity, and more importantly, the training process is stable in comparison to GANs using the JS divergence to measure the distance between the real and generated data distributions. In the future work, we will extend to reconstruct 3D porous structures using the WGAN-GP network and evaluate the synthetic rocks from both geometrical and hydraulic aspects. In particular, we will calculate the permeability of the generated rock samples to analyze the connectivity of pore structures. In addition, to reconstruct multi-scale carbonate rocks, the variational autoencoder will be used to extract microscopic features from SEM images to the synthetic rocks from micro-CT images.

Acknowledgments

We would like to thank Saudi Aramco for funding this research. We would also like to thank King Abdullah University of Science and Technology (KAUST) for providing a license of MATLAB.

References

- Adler, P. M., Jacquin, C. G., & Quiblier, J. A. (1990). Flow in simulated porous media. *International Journal of Multiphase Flow*, **16**(4), 691–712.
- Bera, B., Mitra, S. K., & Vick, D. (2011). Understanding the micro structure of Berea Sandstone by the simultaneous use of micro-computed tomography (micro-CT) and focused ion beam-scanning electron microscopy (FIB-SEM). *Micron*, **42**(5), 412–418.
- Bryant, S. L., King, P. R., & Mellor, D. W. (1993). Network model evaluation of permeability and spatial correlation in a real random sphere packing. *Transport in porous media*, **11**(1), 53–70.
- Blair, S. C., Berge, P. A., & Berryman, J. G. (1996). Using two-point correlation functions to characterize microgeometry and estimate permeabilities of sandstones and porous glass. *Journal of Geophysical Research: Solid Earth*, **101**(B9), 20359–20375.
- Bostanabad, R., Zhang, Y., Li, X., Kearney, T., Brinson, L. C., Apley, D. W., Liu W. K., & Chen, W. (2018). Computational microstructure characterization and reconstruction: Review of the state-of-the-art techniques. *Progress in Materials Science*, **95**, 1–41.
- Chen, C., Hu, D., Westacott, D., & Loveless, D. (2013). Nanometer-scale characterization of microscopic pores in shale kerogen by image analysis and pore-scale modeling. *Geochemistry, Geophysics, Geosystems*, **14**(10), 4066–4075.
- Coelho, D., Thovert, J. F., & Adler, P. M. (1997). Geometrical and transport properties of random packings of spheres and aspherical particles. *Physical Review E*, **55**(2), 1959.
- Dunsmuir, J. H., Ferguson, S. R., D'Amico, K. L., & Stokes, J. P. (1991, October). X-ray microtomography: a new tool for the characterization of porous media. In *SPE annual technical conference and exhibition*. OnePetro.
- Feng, J., He, X., Teng, Q., Ren, C., Chen, H., & Li, Y. (2019). Reconstruction of porous media from extremely limited information using conditional generative adversarial networks. *Physical Review E*, **100**(3), 033308.
- Feng, J., Teng, Q., Li, B., He, X., Chen, H., & Li, Y. (2020). An end-to-end three-dimensional reconstruction framework of porous media from a single two-dimensional image based on deep learning. *Computer Methods in Applied Mechanics and Engineering*, **368**, 113043.
- Flannery, B. P., Deckman, H. W., Roberge, W. G., & D'Amico, K. L. (1987). Three-dimensional X-ray microtomography. *Science*, **237**(4821), 1439–1444.
- Fokina, D., Muravleva, E., Ovchinnikov, G., & Oseledets, I. (2020). Microstructure synthesis using style-based generative adversarial networks. *Physical Review E*, **101**(4), 043308.
- Goodfellow, I., Pouget-Abadie, J., Mirza, M., Xu, B., Warde-Farley, D., Ozair, S., Courville, A., & Bengio, Y. (2014). Generative adversarial nets. *Advances in neural information processing systems*, 27.

- Geiger, S., Cortis, A., & Birkholzer, J. T. (2010). Upscaling solute transport in naturally fractured porous media with the continuous time random walk method. *Water Resources Research*, **46**(12).
- He, X., Santos, R., & Hoteit, H. (2020). Application of machine-learning to construct equivalent continuum models from high-resolution discrete-fracture models. In *International Petroleum Technology Conference*. OnePetro.
- He, X., Sinan, M., Kwak, H., & Hoteit, H. (2021). A Corrected Cubic Law for Single-phase Laminar Flow through Rough-walled Fractures. *Advances in Water Resources*, 103984.
- He, X., Zhu, W., Santos, R., Alsinan, M., Kwak, H., & Hoteit, H. (2021a). CO₂ Leakage Rate Forecasting Using Optimized Deep Learning. In *SPE Annual Technical Conference and Exhibition*. OnePetro.
- He, X., Santos, R., Alsinan, M., Kwak, H., & Hoteit, H. (2021). Constructing Dual-Porosity Models from High-Resolution Discrete-Fracture Models Using Deep Neural Networks. In *SPE Reservoir Simulation Conference*. OnePetro.
- He, X., Zhu, W., Santos, R., Alsinan, M., Kwak, H., & Hoteit, H. (2021b). Fracture Permeability Estimation Under Complex Physics: A Data-Driven Model Using Machine Learning. In *SPE Annual Technical Conference and Exhibition*. OnePetro.
- He, X., Qiao, T., Santos, R., Hoteit, H., AlSinan, M. M., & Kwak, H. T. (2021, November 1). Gas Injection Optimization Under Uncertainty in Subsurface Reservoirs: An Integrated Machine Learning-Assisted Workflow. *ARMA/DGS/SEG 2nd International Geomechanics Symposium*.
- Hoteit, H., & Firoozabadi, A. (2008a). An efficient numerical model for incompressible two-phase flow in fractured media. *Advances in Water Resources*, **31**(6), 891–905.
- Hoteit, H., & Firoozabadi, A. (2008b). Numerical modeling of two-phase flow in heterogeneous permeable media with different capillarity pressures. *Advances in Water Resources*, **31**(1), 56–73.
- Li, Y., Zhang, T., & Sun, S. (2019). Acceleration of the NVT flash calculation for multicomponent mixtures using deep neural network models. *Industrial & Engineering Chemistry Research*, **58**(27), 12312–12322.
- Santos, R., He, X., & Hoteit, H. (2019). Application of machine-learning to construct simulation models from high-resolution fractured formation. In *Abu Dhabi International Petroleum Exhibition & Conference*. OnePetro.
- Santos, R., He, X., Alsinan, M., Kwak, H., & Hoteit, H. (2021). Bayesian Long-Short Term Memory for History Matching in Reservoir Simulations. In *SPE Reservoir Simulation Conference*. OnePetro.
- Zhang, T., Li, Y., Sun, S., & Bai, H. (2020). Accelerating flash calculations in unconventional reservoirs considering capillary pressure using an optimized deep learning algorithm. *Journal of Petroleum Science and Engineering*, **195**, 107886.
- Joshi, M. (1974). A class of stochastic models for porous materials. University of Kansas, Lawrence.
- Legland, D., Ki  u, K., & Devaux, M. F. (2007). Computation of Minkowski measures on 2D and 3D binary images. *Image Analysis & Stereology*, **26**(2), 83–92.
- Liu, S., Zhong, Z., Takbiri-Borujeni, A., Kazemi, M., Fu, Q., & Yang, Y. (2019). A case study on homogeneous and heterogeneous reservoir porous media reconstruction by using generative adversarial networks. *Energy Procedia*, **158**, 6164–6169.
- Mariethoz, G., Renard, P. and Straubhaar, J., 2010. The direct sampling method to perform multiple-point geostatistical simulations. *Water Resources Research*, **46**(11).
- Mosser, L., Dubrule, O., & Blunt, M. J. (2017). Reconstruction of three-dimensional porous media using generative adversarial neural networks. *Physical Review E*, **96**(4), 043309.
- Mosser, L., Dubrule, O., & Blunt, M. J. (2018). Stochastic reconstruction of an oolitic limestone by generative adversarial networks. *Transport in Porous Media*, **125**(1), 81–103.
- Okabe, H., & Blunt, M. J. (2004). Prediction of permeability for porous media reconstructed using multiple-point statistics. *Physical Review E*, **70**(6), 066135.
- Okabe, H., & Blunt, M. J. (2005). Pore space reconstruction using multiple-point statistics. *Journal of petroleum science and engineering*, **46**(1-2), 121–137.
- Okabe, H., & Blunt, M. J. (2007). Pore space reconstruction of vuggy carbonates using microtomography and multiple-point statistics. *Water Resources Research*, **43**(12).
-   ren, P. E., & Bakke, S. (2003). Reconstruction of Berea sandstone and pore-scale modelling of wettability effects. *Journal of petroleum science and engineering*, **39**(3-4), 177–199.
- Otsu, N. (1979). A threshold selection method from gray-level histograms. *IEEE transactions on systems, man, and cybernetics*, **9**(1), 62–66.
- Quiblier, J. A. (1984). A new three-dimensional modeling technique for studying porous media. *Journal of Colloid and Interface Science*, **98**(1), 84–102.
- Roberts, A. P. (1997). Statistical reconstruction of three-dimensional porous media from two-dimensional images. *Physical Review E*, **56**(3), 3203.

- Shams, R., Masihi, M., Boozarjomehry, R. B., & Blunt, M. J. (2020). Coupled generative adversarial and auto-encoder neural networks to reconstruct three-dimensional multi-scale porous media. *Journal of Petroleum Science and Engineering*, **186**, 106794.
- Strebel, S. (2002). Conditional simulation of complex geological structures using multiple-point statistics. *Mathematical geology*, **34**(1), 1–21.
- Tahmasebi, P., & Sahimi, M. (2013). Cross-correlation function for accurate reconstruction of heterogeneous media. *Physical review letters*, **110**(7), 078002.
- Tahmasebi, P., Javadpour, F., & Sahimi, M. (2015). Three-dimensional stochastic characterization of shale SEM images. *Transport in Porous Media*, **110**(3), 521–531.
- Tahmasebi, P. (2017). HYPPS: A hybrid geostatistical modeling algorithm for subsurface modeling. *Water Resources Research*, **53**(7), 5980–5997.
- Tahmasebi, P. (2018). Nanoscale and multiresolution models for shale samples. *Fuel*, **217**, 218–225.
- Valsecchi, A., Damas, S., Tubilleja, C., & Arechalde, J. (2020). Stochastic reconstruction of 3D porous media from 2D images using generative adversarial networks. *Neurocomputing*, **399**, 227–236.
- Volkhonskiy, D., Muravleva, E., Sudakov, O., Orlov, D., Belozerov, B., Burnaev, E., & Koroteev, D. (2019). Reconstruction of 3D porous media from 2D slices. arXiv preprint arXiv:1901.10233.
- Wang, Y.D., Blunt, M. J., Armstrong, R. T., & Mostaghimi, P. (2021). Deep learning in pore scale imaging and modeling. *Earth-Science Reviews*, 103555.
- Zhang, F., Teng, Q., Chen, H., He, X., & Dong, X. (2021). Slice-to-voxel stochastic reconstructions on porous media with hybrid deep generative model. *Computational Materials Science*, **186**, 110018.
- Zhang, T., Xia, P., & Lu, F. (2021). 3D reconstruction of digital cores based on a model using generative adversarial networks and variational auto-encoders. *Journal of Petroleum Science and Engineering*, **207**, 109151.
- Zheng, Q., & Zhang, D. (2020). Digital rock reconstruction with user-defined properties using conditional generative adversarial networks. arXiv preprint arXiv:2012.07719.